THE ASTROPHYSICAL JOURNAL, 553:219–226, 2001 May 20

HIGH-RESOLUTION OBSERVATIONS OF THE MOLECULAR CLOUDS IN THE NGC 1333 IRAS 4 REGION

MINHO CHOI
Institute of Astronomy and Astrophysics, Academia Sinica, Nankang P.O. Box 1-87, Taipei 11529, Taiwan; minho@asiaa.sinica.edu.tw
Received 2000 October 9; accepted 2001 January 18

ABSTRACT

The molecular outflows and the dense cores in the NGC 1333 IRAS 4 region were observed in several molecular lines and in the millimeter continuum with $\sim 4''$ angular resolution. The outflows were particularly well traced by the HCN line. The IRAS 4A northeast-southwestern outflow consists of several compact knots which are spaced regularly and have alternating position angles. This "wiggle" could be produced either by a "precessing" jet or by quasi-periodic outbursts of the driving source. In the former case, the binary separation causing either the precession or the "wobbling" of the protostellar disk should be smaller than the separation between IRAS 4A1 and 4A2. The HCN map shows yet another outflow to the south of IRAS 4A and a compact bipolar outflow driven by IRAS 4BI, but no outflow activity was found near IRAS 4BII. The central velocity of the IRAS 4A dense core is determined to be $V_{LSR} = 6.7$ km s^{-1} using the $C^{18}O$ line. With this central velocity, the optically thick lines toward IRAS 4A are not significantly blue-skewed, and the double-peaked line profile may not be a signature of infall motion in this particular case. IRAS 4BII has a steeper spectral index from 3.4 to 2.7 mm than IRAS 4A/4BI, suggesting that IRAS 4BII may be more evolved than its companions.

Subject headings: ISM: individual (NGC 1333 IRAS 4) — ISM: jets and outflows — ISM: molecules — ISM: structure — stars: formation

1. INTRODUCTION

NGC 1333 IRAS 4 is a well-studied star formation region in the L1450 dark cloud at the distance of 220 pc from the Sun (Černis 1990). There are at least five young stellar objects observed in the dust continuum (Jennings et al. 1987; Sandell et al. 1991; Lay, Carlstrom, & Hills 1995; Looney, Mundy, & Welch 2000). Of particular interest among them is the IRAS 4A binary system, which is driving a well-collimated bipolar outflow (Liseau, Sandell, & Knee 1988; Blake et al. 1995; Hodapp & Ladd 1995). The IRAS 4A outflow shows an interesting directional variability. The CO $J = 3 \rightarrow 2$ map shows that the position angle of the flow changes from about 45° in the large scale ($\sim 4'$) to about 0° near IRAS 4A (Blake et al. 1995). Interferometric observations in the CO $J = 2 \rightarrow 1$ line by Girart, Crutcher, & Rao (1999) show that the position angle of the outflow changes by $\sim 30°$ about $25''$ away from IRAS 4A, and they suggested that the bending is caused by the interaction between the outflowing gas and the magnetic field. Variability may be an important ingredient in understanding how molecular outflows are driven by the protostellar jet/wind (Masson & Chernin 1993; also see the review by Cabrit, Raga, & Gueth 1997 and references therein).

The IRAS 4A molecular core is an interesting case of protostellar collapse candidate. In the HCO^+ survey of class 0 objects, Gregersen et al. (1997) selected good collapse candidates using several selection criteria. IRAS 4A meets the collapse criterion of line asymmetry, almost meets the criterion that the optically thin line peaks at the dip of the optically thick line, and fails the criterion of line peak map because of the strong outflow. Mardones et al. (1997) listed IRAS 4A as one of the spectroscopic infall candidates. An important issue in these studies is the central velocity of the system which is usually measured by observing optically thin lines. Gregersen et al. (1997) used the $H^{13}CO^+$ lines and derived $V_{LSR} = 6.99$–7.06 km s^{-1}. (See Gregersen & Evans 2000 for a discussion on the uncertainty of the $H^{13}CO^+$ line frequency.) Mardones et al. (1997) derived 7.25 km s^{-1} from the N_2H^+ line. However, Blake et al. (1995) derived 6.7 km s^{-1} from the $C^{18}O$ $J = 3 \rightarrow 2$ line, which is bluer than the other two values. This difference is significant because the velocity difference between the peaks of optically thick lines and optically thin lines is only about 0.5 km s^{-1}.

In this paper, we present our high angular resolution observations of the NGC 1333 IRAS 4 region. We report the details of the outflow variability revealed by the HCN line in § 3, new information on the dense molecular core in § 4, and a simple discussion on the dust continuum emission in § 5. A summary is given in § 6.

2. OBSERVATIONS

The NGC 1333 IRAS 4 region was observed using the 10-element BIMA (Berkeley-Illinois-Maryland Association) array in two frequency bands. The lower frequency band, including the $\lambda = 3.4$ mm continuum, the HCN $J = 1 \rightarrow 0$ line, and the HCO^+ $J = 1 \rightarrow 0$ line, was observed in the B-array configuration in 1999 February, and the resulting data were combined with the C-array data presented previously (Choi, Panis, & Evans 1999). The higher frequency band, including the $\lambda = 2.7$ mm continuum, the $C^{18}O$ $J = 1 \rightarrow 0$ line, and the ^{13}CO $J = 1 \rightarrow 0$ line, was observed in the B- and the D-array configurations in 1999 March and in the C-array configuration in 1999 April. For the lower frequency band observations, the phase tracking center was the same as that used by Choi et al. (1999). For the higher frequency band observations, the phase tracking center was $\alpha_{2000} = 03^h29^m10^s.44$ and $\delta_{2000} = 31°13'31''.5$, which is also the central position of the maps presented in this paper. The phase was determined by observing nearby quasars 3C 84 and QSO J0237+2848. The flux calibration was done by observing Venus and Uranus.

For the molecular lines, the spectral windows were set to a resolution of 0.049 MHz giving a velocity resolution of

0.16 km s^{-1} in the lower frequency band and 0.13 km s^{-1} in the higher frequency band. The continuum was subtracted from the visibility data of the lines, using the visibility reconstructed from the CLEAN maps of the continuum. All maps were made using a CLEAN algorithm. The angular resolutions are given in figure legends.

3. HCN OUTFLOWS

The outflow will be discussed based on the HCN data because the HCN line shows line wing emission much more enhanced than the other lines observed (see the HCO^+ outflow map presented by Choi et al. 1999). However, the frequency separations between the hyperfine components of the HCN line are comparable to the width of the line wing. As a result, the analysis of the kinematics is complicated because of the blending of hyperfine components, and the discussion will be mainly based on the outflow morphology. Figure 1 shows the map of the line wing emission and the positions of the HCNOP[1] objects. Figure 2 shows the HCN spectra at the outflow peaks. At HCNOP 3/4, the redshifted line wing may extend beyond the spectral coverage. The absorption-like feature at 8 km s^{-1} of each hyperfine component is the "redshifted null" which will be discussed in § 4.2. Although the CO $J = 2 \rightarrow 1$ map of Girart et al. (1999) and the HCN map in this paper have comparable beam sizes, the HCN map shows more detailed structure of the

[1] Following the IAU designation convention, we recommend that the HCN outflow peaks in Fig. 1 may be named using the acronym of HCNOP. For example, the second peak north of IRAS 4A may be referred to as HCNOP 3.

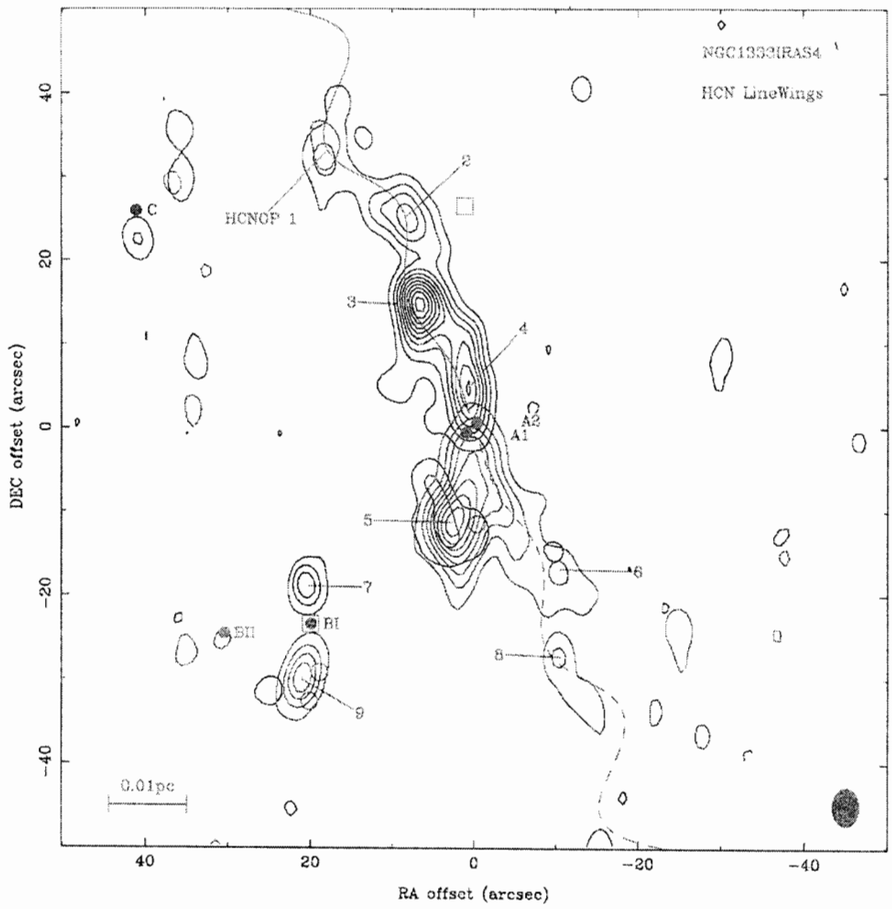

FIG. 1.—Map of the HCN $J = 1 \rightarrow 0$ line wings toward the NGC 1333 IRAS 4 region. The HCN line was averaged over the V_{LSR} (km s^{-1}) intervals of (-11.7, -1.3) and (2.1, 5.8) for blue contours and over (9.2, 10.6) and (14.0, 21.6) for red contours. Velocities are relative to the rest frequency of the $F = 2 \rightarrow 1$ component. The gaps in the velocity intervals are the line core velocities of the other hyperfine components. The blue contours represent the blueshifted emission of the $F = 2 \rightarrow 1$ component with some contamination from the $F = 0 \rightarrow 1$ component, and the red contours represent the redshifted emission of the $F = 2 \rightarrow 1$ component with some contamination from the $F = 1 \rightarrow 1$ component. The lowest contour level and the contour interval are 0.05 Jy beam^{-1}. Names of the HCN outflow peaks (HCNOPs) discussed in the text are written in the figure (see § 3). Shown at the bottom right-hand corner is the synthesized beam: FWHM = 4.″6 × 3.″3 and P.A. = 0°. The filled circles mark the millimeter/submillimeter continuum sources (Looney et al. 2000; Smith et al. 2000). The open squares mark the H_2O maser sources (Haschick et al. 1980; Moran 1983). The open circles mark the nebulous sources in the H_2 1–0 $S(1)$ emission: source 6 near HCNOP 5 and double source 9 near HCNOP 9 (Hodapp & Ladd 1995). The curved line connects points where the position angle is a sinusoidal function of the angular distance from the map center (see § 3.1). The straight line at the bottom left-hand corner corresponds to 0.01 pc at the distance of 220 pc.

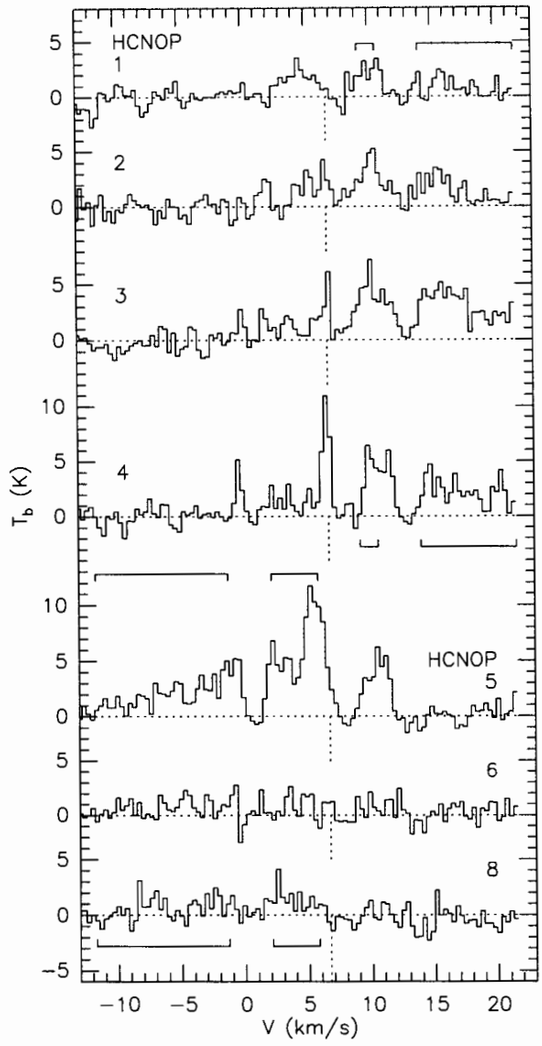

FIG. 2.—HCN line spectra toward the outflow peaks shown in Fig. 1. To see the line wings clearly, the spectra were smoothed to degrade the spectral resolution by a factor of 2. The vertical dotted line marks V_{LSR} = 6.7 km s^{-1} for each hyperfine component. The horizontal brackets show the velocity intervals for the contour maps in Fig. 1.

outflow, probably because of the abundance enhancement (Blake et al. 1995). It is also possible that, in interferometer maps, the HCN line may be more sensitive to the contrast of excitation conditions (such as density) than the CO line. The HCN map shows at least three outflows: IRAS 4A northeast-southwestern (NE-SW) outflow (containing HCNOP 1/2/3/4 and HCNOP 6/8), IRAS 4A southern outflow (HCNOP 5), and IRAS 4BI outflow (HCNOP 7/9).

3.1. *IRAS 4A NE-SW Bipolar Outflow*

The NE-SW outflow consists of a series of compact knots. With the beam size of Figure 1, it is difficult to tell which object in the IRAS 4A1/2 system is the driving source of this flow. The compact nature of the outflow knots and the high degree of collimation suggest that these knots are intimately connected with the jet/wind driving the molecular outflow. A close examination of the spatial distribution of the knots, especially those in the red lobe, reveals two interesting facts: a nearly regular spacing between knots and alternating changes of position angle.

To show this "wiggle" pattern clearly, a curve is drawn in Figure 1 according to the equation $\theta = \theta_0 + \theta_w \sin(\omega d + \phi)$, where θ and d are the position angle and the angular distance relative to the driving source. The constants θ_0, θ_w, ω, and ϕ were derived by fitting HCNOP 1/2/3 to the extrema of the curve. HCNOP 4 was not included in the fit because of its proximity to the driving source. The derived amplitude is $\theta_w \approx 5°$, and the wavelength is $22'' \pm 1''$. Assuming that the outflow is close to the plane of the sky and that the jet/wind speed is ~ 100 km s^{-1} (here we are only interested in the order of magnitude estimates), the period of the wiggle is $P_w \approx 220$ yr. All the four HCNOP 1/2/3/4 knots coincide with the extrema of the curve within the beam size of the map. If the curve is rotated around the map center by 180° (*dashed curve*), it fits HCNOP 6/8 surprisingly well, which suggests that the wiggle has a point symmetry.

Assuming the HCN abundance of 3.8×10^{-8} (Blake et al. 1995), the mass contained in each redshifted knot is (1–3) $\times 10^{-3}$ $M_\odot$. This estimate can be highly uncertain because the abundance enhancement relative to the line core (factor of ~ 240) can change along the outflow. It would be interesting to know the kinematics of the wiggling outflow, which is difficult to get with the HCN line because of the hyperfine structure.

3.1.1. *Directional Variability*

Outflow variability can be caused by many different physical mechanisms: intrinsic variability of the driving source, instability in the driving jet/wind, or influence of external environment. The periodic nature of the wiggle rules out external perturbations, such as the external magnetic field suggested by Girart et al. (1999). Among the previously proposed variability mechanisms, we will examine three of them which can produce periodic variability of the jet direction. The first two are intrinsic to the driving source, and the third one is due to the jet instability.

Precessing disk.—Since the driving mechanism of protostellar outflow is thought to be closely related to the protostellar disk, "precession" of outflow axis is expected if the driving source belongs to a binary system and if the protostellar disk is misaligned with the orbital plane of the binary (Papaloizou & Terquem 1995; Terquem et al. 1999). The precession period would be of order 20 times the binary orbital period (see Bate et al. 2000 and references therein). If the wiggle in the NE-SW outflow is caused by the precession of the disk, the expected orbital period would be $P_b \approx 11$ yr.

Wobbling disk.—If the protostellar disk is not perfectly rigid, the tidal force of the companion can cause the disk to wobble with a period of $\sim P_b/2$ (Bate et al. 2000). In this case, the expected orbital period would be $P_b \approx 450$ yr.

For the IRAS 4A1/2 system, assuming the total mass of 0.9 $M_\odot$ (see § 5), the projected separation of 1".7 gives $P_b >$ 7600 yr. Therefore the interaction between IRAS 4A1 and 4A2 cannot cause the wiggle by either precession or wobbling. Then it is likely that one component of the IRAS 4A1/2 system is itself a close binary system. Assuming that

this close binary system has half the total mass of the IRAS 4A1/2 system, the expected binary separation would be ~4 AU (0".02) in the case of the precessing disk or ~45 AU (0".2) in the case of the wobbling disk.

Kelvin-Helmholtz instability.—A periodic wiggle can be produced by the growth of the sinusoidal mode of the Kelvin-Helmholtz instability, and the expected period of the wiggle is ~200 years for typical protostellar jet parameters (Stone, Xu, & Hardee 1997). The numerical simulations typically show that it takes several cycles from the driving source to fully develop the instability, while the NE-SW outflow shows the wiggle right away from the driving source. In addition, with the jet instability, it is difficult to explain the point symmetry seen in the NE-SW outflow.

3.1.2. *Intensity Variability*

The regular spacing between outflow knots can be explained by two different possibilities. (1) A steady flow with "precession" can produce peaks with alternating position angle because of the projection effect (Raga, Cantó, & Biro 1993). In this model, the intensity of the condensation would increase with the distance from the driving source, which is the opposite of what is observed along the NE-SW outflow. (However, Raga et al. 1993 considered the intensity of the Hα line, not molecular lines.) (2) Episodic ejection of material by (quasi-)periodic outbursts of the central source (for example, FU Ori outburst) can explain the regular spacing between knots. It is not clear, however, how such outbursts can produce the directional variability in phase with the intensity variability, as in the NE-SW outflow.

In principle, the two possibilities above can be tested observationally. First, if the knots are resolved with a high angular resolution, arclike shapes pointing away from the outflow axis are expected from the possibility (1), while bow shocks pointing away from the driving source are expected from the possibility (2). Second, if the possibility (2) is the case, the brightness variation of the central source may be detectable: currently the outburst may be in the decay phase, and the next outburst may occur 60 ± 25 yr from now.

3.1.3. *Large-Scale Variability*

There is a ~12° difference in the position angle between the central axis of the HCN outflow (θ_0) and the large-scale CO/H_2 outflow (Blake et al. 1995; Hodapp & Ladd 1995). Does this difference mean that there is a directional variability with a timescale longer than that of the wiggle in the HCN map? Only a large-scale map with a high angular resolution can answer this question, but we may speculate that multiple mode of directional variability may exist in one outflow, caused either by different mechanisms (for example, precession and wobbling of disk) or by a hierarchical triple system (i.e., the closer companion of the driving source responsible for the shorter period variability and the farther companion responsible for the longer period variability).

3.2. *IRAS 4A Southern Outflow*

This outflow shows a strong blueshifted peak at HCNOP 5. (The red contours near HCNOP 5 in Fig. 1 are due to the blueshifted emission of the $F = 1 \rightarrow .1$ hyperfine component.) This flow is separate from the NE-SW outflow. A candidate driving source would be one of the objects in the IRAS 4A binary system. Then a redshifted counterpart is expected to the north of IRAS 4A, but no such outflow can be seen in the HCN map. A possible hint to the counterpart could be the H_2O maser source 27″ north of IRAS 4A and

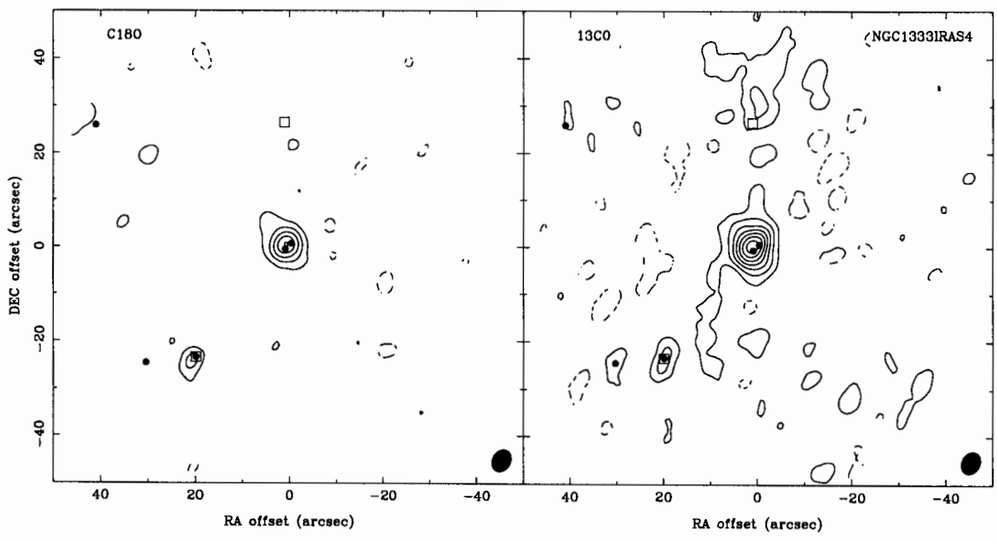

FIG. 3.—Maps of the $C^{18}O$ and the ^{13}CO $J = 1 \rightarrow 0$ lines. The lowest contour level and the contour interval are 0.23 Jy beam^{-1}. Dashed contours are for negative levels. The $C^{18}O$ line was averaged over the velocity interval of 5.9–7.4 km s^{-1}, and the synthesized beam is FWHM = 5".0 × 4".0 and P.A. = −32°. The ^{13}CO line was averaged over the velocity interval of 5.8–7.1 km s^{-1}, and the synthesized beam is FWHM = 4".8 × 3".9 and P.A. = −32°. The filled circles mark the dust continuum sources, and the open squares mark the H_2O maser sources (see Fig. 1).

the ambient-velocity ^{13}CO emission around it (Fig. 3). Since the HCNOP 5 outflow is relatively short, the object responsible for this outflow could have started outflow activity only recently relative to the other one responsible for the NE-SW outflow.

3.3. *IRAS 4B Outflow*

Figure 1 shows that the blueshifted and the redshifted lobes of the IRAS 4BI outflow are clearly separated, and the outflow axis is almost exactly in the north-south direction. Assuming the jet/wind velocity of 100 km s^{-1}, the dynamical timescale is only ~ 120 years, which suggests that IRAS 4BI is an extremely young object.

Lefloch et al. (1998) suggested that IRAS 4B may be the driving source of the H_2 jet (detected by Hodapp & Ladd 1995) located inside a large-scale cavity (Cav2) of their millimeter continuum map. However, since this H_2 jet (hereafter "Cav2 jet") is propagating to the west, very different from the direction of the IRAS 4BI molecular outflow, it is unlikely that IRAS 4BI is the driving source of the Cav2 jet. An alternative possibility is that the driving source of the Cav2 jet may be IRAS 4BII. (The existence of IRAS 4BII was not known when Lefloch et al. 1998 presented their analysis.) If this is the case, the relatively large extent of the Cav2 jet suggests that IRAS 4BII could be more evolved than IRAS 4BI. See § 5 for further discussions on the evolutionary stage of the protostellar sources.

4. THE MOLECULAR CORE

Figures 3 and 4 show the maps of the molecular lines. Figure 5 shows the spectra toward IRAS 4A. Channel maps of the HCO^+ and the HCN lines in a lower angular resolution were presented by Choi et al. (1999). The $C^{18}O$ and the ^{13}CO lines trace the compact cores around the millimeter continuum sources. The HCO^+ and the HCN lines trace more extended gas including a bridgelike structure between IRAS 4A and 4BI. The dense cores around IRAS 4A and 4BI were detected in all the molecular lines observed. A small molecular core near IRAS 4BII can be seen in the ^{13}CO map.

The kinematics of the IRAS 4A core will be discussed below, and this discussion applies to the IRAS 4BI core qualitatively in the same way.

4.1. *Central Velocity*

Chemistry models suggest that N_2H^+ is a better tracer of the dense core than other molecules (for example, see Bergin & Langer 1997). Toward IRAS 4A, however, the N_2H^+ line profile is wide (FWHM = 1.32 km s^{-1}) and flat-topped (Mardones et al. 1997), which suggests that the N_2H^+ line is either optically thick or composed of multiple velocity components. Since there are strong outflows near the central object (for example, HCNOP 4 is only 5″ away from IRAS 4A), previous single-dish observations could have been affected by the outflow.

A safe way to determine the central velocity would be observing in a molecular line insensitive to the outflow with a high angular resolution. In this sense, the $C^{18}O$ spectrum (Fig. 5*a*) may give the best estimate of the central velocity so far. The map (Fig. 3) shows that the $C^{18}O$ line traces a compact structure centered at the IRAS 4A system. A Gaussian fit to the $C^{18}O$ $J = 1 \rightarrow 0$ spectrum gives the central velocity of 6.69 ± 0.03 km s^{-1} with the FWHM of

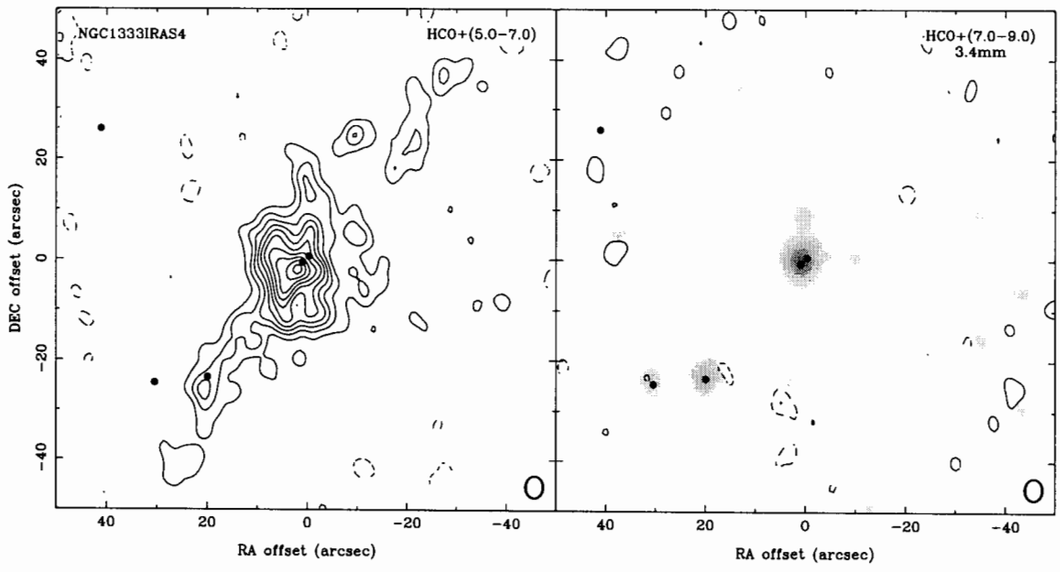

FIG. 4.—Maps of the HCO^+ $J = 1 \rightarrow 0$ line. The lowest contour level and the contour interval are 0.13 Jy $beam^{-1}$. The HCO^+ line was averaged over the velocity intervals of 5.0–7.0 km s^{-1} (*left panel*) and 7.0–9.0 km s^{-1} (*right panel*). Shown in gray scale is the $\lambda = 3.4$ mm continuum map. The gray scale starts from 11 mJy $beam^{-1}$. The synthesized beams are FWHM = 4.″3 × 3.″4 and P.A. = −3° for the HCO^+ line and FWHM = 4.″4 × 3.″7 and P.A. = −3° for the continuum.

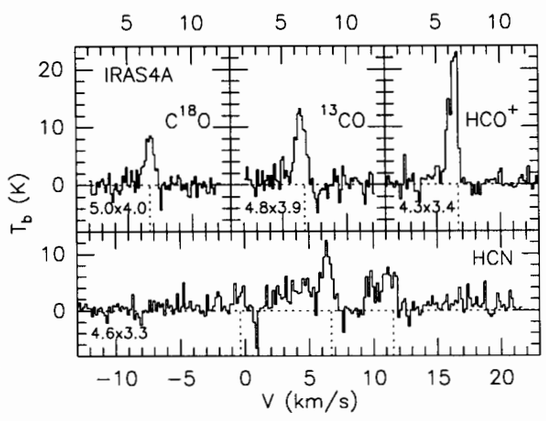

FIG. 5a

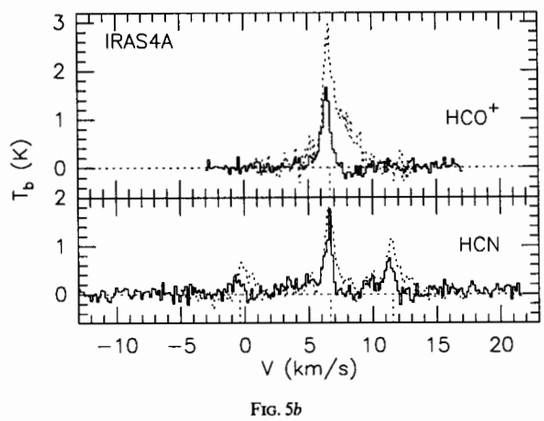

FIG. 5b

FIG. 5.—Molecular line spectra toward NGC 1333 IRAS 4A. The vertical dotted line marks $V_{LSR} = 6.7$ km s^{-1}. (*a*) Spectra from the BIMA data. Shown at the bottom left-hand corner are the synthesized beam sizes in arcseconds. (*b*) The HCO^+ and the HCN line spectra with an angular resolution of 70″. Solid spectra are from the BIMA maps convolved with a Gaussian beam. Dotted spectra were obtained using the NRAO 12 m telescope.

0.79 ± 0.08 km s^{-1}. Therefore the central velocity of the IRAS 4A dense core is most likely to be 6.7 km s^{-1}, in agreement with Blake et al. (1995).

To quantify the line profile as a measure of collapse signature, Gregersen et al. (1997) used the skewness of the HCO^+ lines, and Mardones et al. (1997) used the nondimensional velocity difference, δV, of the CS and the H_2CO lines. They obtained negative (blue) values of these collapse indicators for IRAS 4A and 4BI. Taking 6.7 km s^{-1} as the central velocity, however, the collapse indicators would become nearly zero (even slightly positive for δV_{CS}). This does not necessarily rule out the existence of infalling motion in the core, but it could mean that the collapse may not be the dominant component of the cloud kinematics.

4.2. *Redshifted Null*

A characteristic feature of the interferometric maps of this region is the lack of emission in about 2 km s^{-1} wide velocity interval around $\sim$8 km s^{-1} (hereafter "redshifted null"). This feature is severe in the HCO^+ and the HCN lines (Fig. 4), and even the ^{13}CO spectrum shows this feature (Fig. 5*a*). As a result, optically thick lines show very asymmetric line profiles. In order to find out whether the redshifted null is caused by the missing flux at this particular velocity interval or by the absorption in the infalling cold envelope, spectra of the HCN and the HCO^+ lines were obtained using the NRAO (National Radio Astronomy Observatory) 12 m telescope at Kitt Peak in 1998 December and in 1999 February. Comparison of the spectra at the same angular resolution (Fig. 5*b*) shows that a significant fraction of the flux at the redshifted null was lost in the BIMA observations while most of the flux on the blueshifted side was recovered.

Is the missing flux problem caused by the envelope of the IRAS 4 dense cores or by an unrelated cloud? Useful information can be found in the single-dish observations of the CS $J = 3 \rightarrow 2$ line (Langer, Castets, & Lefloch 1996). At 6.5 km s^{-1}, the CS channel map shows a compact peak at IRAS 4. At 8 km s^{-1}, however, IRAS 4 lies in a valley between the two emission ridges extended from the SVS 13 region, which may have aggravated the missing flux problem in the BIMA maps. This extended cloud at 8 km s^{-1} may also be responsible for the redshifted peak of the optically thick lines in the single-dish observations. For more discussions on the relation between the two cloud components, see Langer et al. (1996) and Lefloch et al. (1998).

5. DUST CONTINUUM

Table 1 lists the continuum fluxes of the compact objects, and Figure 4 shows the $\lambda = 3.4$ mm continuum map. The continuum peak positions and fluxes agree well with previous observations (Choi et al. 1999; Looney et al. 2000). The contribution from free-free emission (Rodríguez, Anglada, & Curiel 1999) is negligible at millimeter wavelength. To derive the mass from the dust continuum flux, the dust emissivity given by Beckwith & Sargent (1991) is assumed,

$$\kappa_\nu = 0.1\left(\frac{\nu}{\nu_0}\right)^\beta \text{ cm}^2 \text{ g}^{-1}\,, \tag{1}$$

where $\nu_0 = 1200$ GHz, and β is the opacity index. Assuming optically thin emission from single-temperature dust, the mass can be estimated by

$$M_d = \frac{F_\nu D^2}{\kappa_\nu B_\nu(T_d)}\,, \tag{2}$$

where F_ν is the flux density, D is the distance to the source, B_ν is the Planck function, and T_d is the dust temperature. Table 2 lists the β and mass derived from the fluxes given in Table 1 with the assumption of $T_d = 33$ K (Jennings et al. 1987). The uncertainty estimates of the mass in Table 2 do not include the contribution from the uncertainties of D, T_d, and the factor 0.1 in equation (1).

TABLE 1

MILLIMETER CONTINUUM SOURCES IN THE NGC 1333 IRAS 4 REGION

	PEAK POSITION[a]		PEAK FLUX[b]		TOTAL FLUX[c]	
SOURCE	α_{2000}	δ_{2000}	3.4 mm	2.7 mm	3.4 mm	2.7 mm
IRAS 4A.....	03 29 10.5	31 13 32	227 ± 4	469 ± 9	303	604
IRAS 4BI[d].....	03 29 12.0	31 13 08	96 ± 4	177 ± 12	104	212
IRAS 4BII[d].....	03 29 12.8	31 13 07	36 ± 5	87 ± 14	40	102

NOTE.—Units of right ascension are hours, minutes, and seconds, and units of declination are degrees, arcminutes, and arcseconds. Fluxes are corrected for the primary beam response. IRAS 4C (VLA 29) was not detected in our continuum maps.

[a] Positions are from the $\lambda = 2.7$ mm map (synthesized beam FWHM = 4.″6 × 3.″7).

[b] Peak flux in mJy beam^{-1}.

[c] Integrated flux in mJy from a Gaussian fit to pixels above 4 σ level.

[d] This paper follows the nomenclature of Smith et al. 2000, as marked in Fig. 1. IRAS 4BI/4BII were referred to as IRAS 4B/4C by Looney et al. 2000.

Dent, Matthews, & Ward-Thompson (1998) showed that class 0 objects typically have $\beta = 1.0$–1.5, all the class I objects have $\beta = 1.0$–2.0, and most of the optically visible T Tauri stars have $\beta = 0.0$–1.0. From the submillimeter data given by Sandell et al. (1991), Dent et al. (1998) listed IRAS 4A as a class 0 object with an unusually low β (~ 0.5). In contrast, our estimate at millimeter wavelength shows that the β of IRAS 4A (~ 0.9) is not far from the typical β of class 0 objects. The low β at shorter wavelength could mean that the submillimeter continuum of IRAS 4A may have a moderate optical depth. The mass estimates of IRAS 4A and 4BI are consistent with those of Looney et al. (2000) scaled to the same distance.

IRAS 4BII seems to have characteristics different from its companions; its β is significantly higher (Table 2), and there is no molecular outflow associated with it (see § 3.3 for the possibility of an ancient outflow activity). This could imply that IRAS 4BII may be in an evolutionary stage different from the other two sources. To explain the compact nature of IRAS 4BII, Looney et al. (2000) suggested that it could be an optical/IR source. (IRAS 4BII was referred to as IRAS 4C by Looney et al. 2000.) However, the high β (~ 1.9) suggests that IRAS 4BII is more similar to a class I object rather than an optically visible T Tauri star (Dent et al. 1998). The mass estimate of IRAS 4BII is higher than that of Looney et al. (2000) mainly because they assumed $\beta = 1$. There is a possibility that the dust temperature assumed in our calculations may be inappropriate for IRAS 4BII because Jennings et al. (1987) derived the temperature for the whole IRAS 4 system. If $T_d = 100$ K is assumed, to illustrate the dependency on T_d, the derived mass of IRAS 4BII becomes 0.6 $M_\odot$.

TABLE 2

SPECTRAL INDEX AND MASS FROM THE DUST CONTINUUM

Source	Spectral Index (α)	Opacity Index (β)	Mass ($M_\odot$)
IRAS 4A	2.80 ± 0.09	0.87	$0.9^{+0.3}_{-0.2}$
IRAS 4BI.....	2.9 ± 0.3	1.0	$0.4^{+0.4}_{-0.2}$
IRAS 4BII	3.8 ± 0.8	1.9	$1.7^{+10.6}_{-1.5}$
IRAS 4BII[a].....	3.9 ± 0.3	1.9	$2.1^{+2.4}_{-1.2}$

[a] Including the $\lambda = 6.9$ mm total flux of 2.6 ± 0.3 mJy from the recent VLA (Very Large Array) observations by J. Lim & C. L. Carilli (2000, private communication).

Within the IRAS 4 cluster, IRAS 4BI and 4BII are relatively close to each other with a projected separation of ~ 2300 AU. Judging from their spectral indices and the dynamical timescale of the IRAS 4BI outflow, however, they are in quite different evolutionary stages; IRAS 4BI may be a class 0 object only a few hundred years old, while IRAS 4BII may be a class I object. A typical lifetime of class I objects is $\sim 10^5$ years (André & Montmerle 1994). This illustrates that closer companions in a protostellar cluster are not necessarily in a relatively similar evolutionary stage.

6. SUMMARY

The NGC 1333 IRAS 4A region was observed in several molecular lines and in the millimeter continuum with a $\sim 4''$ angular resolution. The HCN map shows three molecular outflows: two driven by the IRAS 4A binary system and the other driven by IRAS 4BI.

The IRAS 4A northeast-southwestern outflow shows a wiggling flow pattern. Assuming the flow velocity of 100 km s^{-1}, the period of the wiggle is ~ 220 years. The wiggle seems to show a point symmetry about the driving source. The wiggle can be explained either by a steady outflow with precessing flow axis or by periodic outbursts of the driving source. If the wiggling outflow is due to the precession or the wobbling of a protostellar disk caused by the tidal interaction in a binary system, the predicted binary separation is much smaller than the separation between IRAS 4A1 and 4A2, suggesting that IRAS 4A could be a hierarchical triple system.

The IRAS 4BI outflow has a short (~ 120 years) dynamic timescale, which suggests that the star formation activity of IRAS 4BI has started relatively recently. IRAS 4BII does not show any outflow activity currently, but it could be the driving source of the ancient outflow responsible for the Cav2 cavity proposed by Lefloch et al. (1998).

The C^{18}O map shows a compact core at IRAS 4A. The C^{18}O line profile is centered at $V_{LSR} = 6.7$ km s^{-1} and narrower than the other lines previously observed toward IRAS 4A. Therefore we suggest that the central velocity of the system is 6.7 km s^{-1} and that the previously suggested spectral infall signature of IRAS 4A should be reconsidered. Though the star formation activities such as the outflow strongly imply the existence of infall motion, the line profiles of optically thick lines may be influenced by other motions and multiple velocity components.

Comparison of the $\lambda = 3.4$ and 2.7 mm continua shows that IRAS 4BII has a significantly steeper spectrum than IRAS 4A and 4BI. This implies that IRAS 4BII may be a class I object while IRAS 4A and 4BI are class 0 objects with a relatively low opacity index.

We thank A. Allen, N. J. Evans II, E. M. Gregersen, J. Lim, N. Ohashi, S. P. Willner, and C. Yuan for helpful discussions. We acknowledge partial support from NSF grant AST 96-13716 and from the Frank Kerr Fellowship.

REFERENCES

André, P., & Montmerle, T. 1994, ApJ, 420, 837
Bate, M. R., Bonnell, I. A., Clarke, C. J., Lubow, S. H., Ogilvie, G. I., Pringle J. E., & Tout, C. A. 2000, MNRAS, 317, 773
Beckwith, S. V. W., & Sargent, A. I. 1991, ApJ, 381, 250
Bergin, E. A., & Langer, W. D. 1997, ApJ, 486, 316
Blake, G. A., Sandell, G., van Dishoeck, E. F., Groesbeck, T. D., Mundy, L. G., & Aspin, C. 1995, ApJ, 441, 689
Cabrit, S., Raga, A., & Gueth, F. 1997, in IAU Symp. 182, Herbig-Haro Flows and the Birth of Low-Mass Stars, ed. B. Reipurth & C. Bertout (Dordrecht: Kluwer), 163
Černis, K. 1990, Ap&SS, 166, 315
Choi, M., Panis, J.-F., & Evans, N. J., II 1999, ApJS, 122, 519
Dent, W. R. F., Matthews, H. E., & Ward-Thompson, D. 1998, MNRAS, 301, 1049
Girart, J. M., Crutcher, R. M., & Rao, R. 1999, ApJ, 525, L109
Gregersen, E. M., & Evans, N. J., II 2000, ApJ, 538, 260
Gregersen, E. M., Evans, N. J., II, Zhou, S., & Choi, M. 1997, ApJ, 484, 256
Haschick, A. D., Moran, J. M., Rodríguez, L. F., Burke, B. F., Greenfield, P., & Garcia-Barreto, J. A. 1980, ApJ, 237, 26
Hodapp, K.-W., & Ladd, E. F. 1995, ApJ, 453, 715
Jennings, R. E., Cameron, D. H. M., Cudlip, W., & Hirst, C. J. 1987, MNRAS, 226, 461
Langer, W. D., Castets, A., & Lefloch, B. 1996, ApJ, 471, L111
Lay, O. P., Carlstrom, J. E., & Hills, R. E. 1995, ApJ, 452, L73
Lefloch, B., Castets, A., Cernicharo, J., & Loinard, L. 1998, ApJ, 504, L109
Liseau, R., Sandell, G., & Knee, L. B. G. 1988, A&A, 192, 153
Looney, L. W., Mundy, L. G., & Welch, W. J. 2000, ApJ, 529, 477
Mardones, D., Myers, P. C., Tafalla, M., Wilner, D. J., Bachiller, R., & Garay, G. 1997, ApJ, 489, 719
Masson, C. R., & Chernin, L. M. 1993, ApJ, 414, 230
Moran, J. M. 1983, Rev. Mexicana Astron. Astrofis., 7, 95
Papaloizou, J. C. B., & Terquem, C. 1995, MNRAS, 274, 987
Raga, A. C., Cantó, J., & Biro, S. 1993, MNRAS, 260, 163
Rodríguez, L. F., Anglada, G., & Curiel, S. 1999, ApJS, 125, 427
Sandell, G., Aspin, C., Duncan, W. D., Russell, A. P. G., & Robson, E. A. 1991, ApJ, 376, L17
Smith, K. W., Bonnell, I. A., Emerson, J. P., & Jenness, T. 2000, MNRAS, 319, 991
Stone, J. M., Xu, J., & Hardee, P. E. 1997, ApJ, 483, 136
Terquem, C., Eislöffel, J., Papaloizou, J. C. B., & Nelson, R. P. 1999, ApJ, 512, L131